

[Chapter 5: Synthesis of $\text{La}_{0.67}\text{Sr}_{0.33}\text{Mn}_{1-x}\text{Fe}_x\text{O}_3$ ($x=0.15, 0.25$ and 0.35) materials prepared by Sol-Gel method]

5.1 Introduction

The perovskite manganese oxides are considered as a processing material for spintronics due to highly spin polarized carriers in them and the colossal magnetoresistivity [1-4]. The properties of manganese oxides get modified due to several reasons, the structure-property relation being the most important. The structure property relation of a material depends on synthesis route. Keeping this in mind, in present chapter, we have studied the structural, morphological, electronic and vibrational properties of sol-gel synthesized Fe doped $\text{La}_{0.67}\text{Sr}_{0.33}\text{MnO}_3$ manganites.

The sol-gel method was developed in the 1960s mainly due to the need of new synthesis methods in the nuclear industry. A method was needed where dust was reduced (compared to the ceramic method) and needed a lower sintering temperature. In addition, it should be possible to do the synthesis by remote control.

Sol-gel technology to synthesize materials is a well known colloidal chemistry technology, which produces various materials with novel and predefined properties. This is a simple and low cost method. The sol is a name of a colloidal solution made of solid particles within few hundred nanometer (nm) in diameter suspended in a liquid phase. Hence, it plays a principle role in the development of modern nanotechnology for the preparation of new materials. However, the gel is a solid macromolecule immersed in a solvent. Both liquid and solid are diffused in each other. The application of the sol-gel method and flow chart of the preparation of nanoparticles using sol-gel technique is displayed in Fig. 5.1 and 5.2 respectively.

[Chapter 5: Synthesis of $\text{La}_{0.67}\text{Sr}_{0.33}\text{Mn}_{1-x}\text{Fe}_x\text{O}_3$ ($x=0.15, 0.25$ and 0.35) materials prepared by Sol-Gel method]

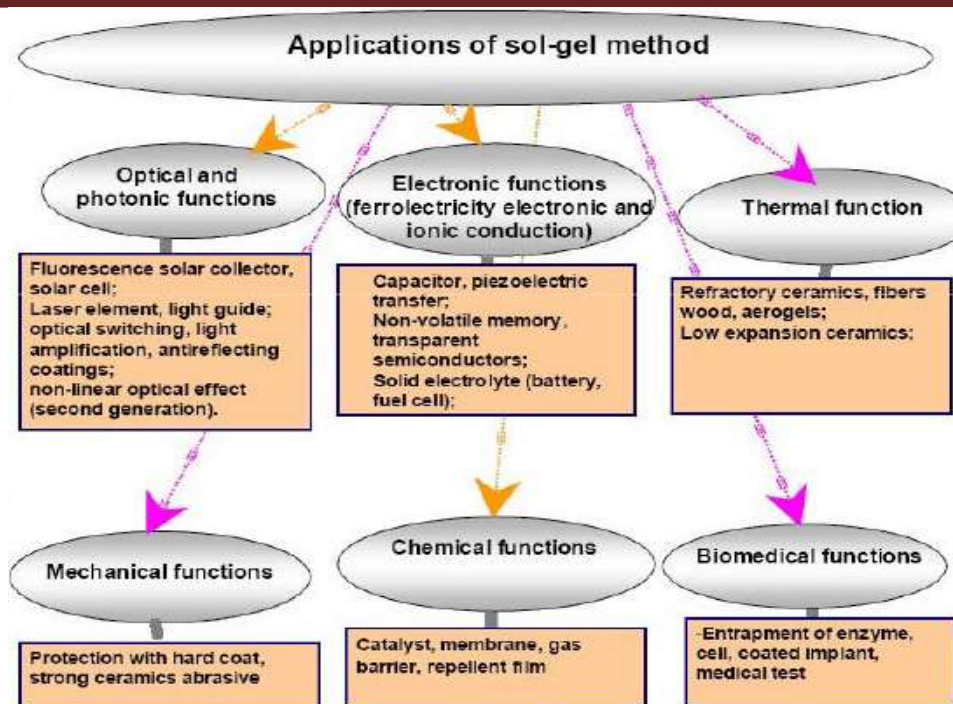


Fig. 5.1: Application chart of the Sol-Gel method [5].

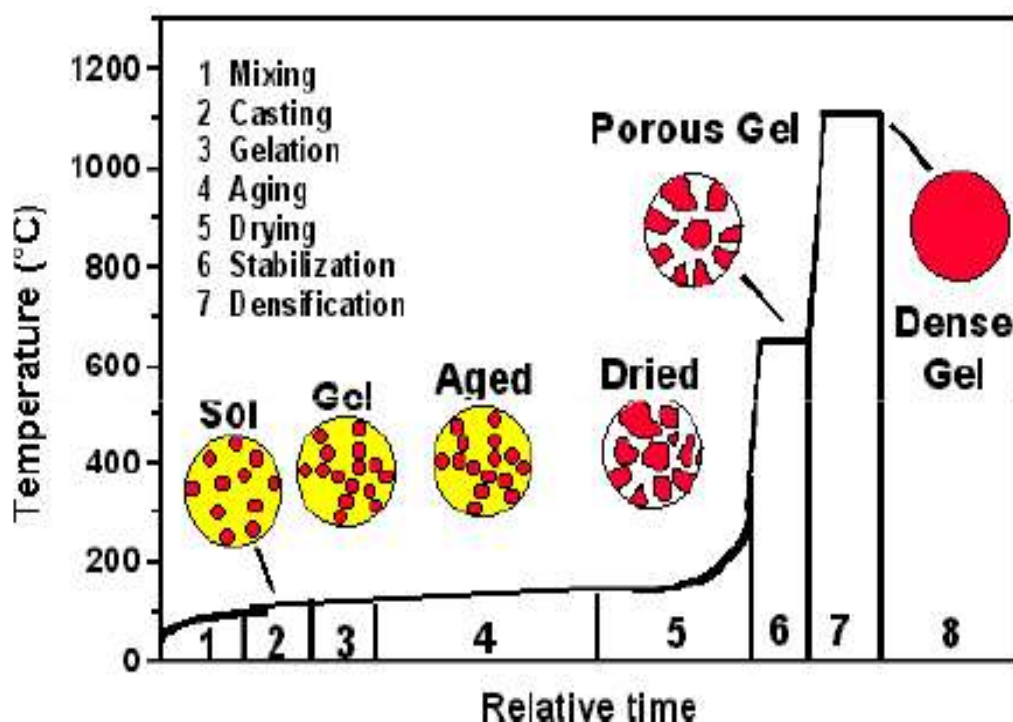


Fig. 5.2: Processing of nanoscale particle by sol-gel method [6].

[Chapter 5: Synthesis of $\text{La}_{0.67}\text{Sr}_{0.33}\text{Mn}_{1-x}\text{Fe}_x\text{O}_3$ ($x=0.15, 0.25$ and 0.35) materials prepared by Sol-Gel method]

5.2 Methodology and Experimental Details

The $\text{La}_{0.67}\text{Sr}_{0.33}\text{Mn}_{1-x}\text{Fe}_x\text{O}_3$ (LSMFO, $x= 0.15, 0.25$ and 0.35) samples prepared in this section are named as samples LSMFO-0.15, LSMFO-0.25 and LSMFO-0.35 respectively for $x= 0.15, 0.25$ and 0.35 . In this study, all reagents have been of analytical grade (AR). The LSMFO nanoscale particles $\text{La}_{0.67}\text{Sr}_{0.33}\text{Mn}_{1-x}\text{Fe}_x\text{O}_3$ (with $x= 0.15, 0.25$ and 0.35) were synthesized using their nitrate precursors. AR grade starting compounds in stoichiometric amounts of lanthanum nitrate $\text{La}(\text{NO}_3)_3 \cdot 6\text{H}_2\text{O}$ (purity $\geq 99.0\%$), strontium nitrate $\text{Sr}(\text{NO}_3)_2$ (purity $\geq 99.5\%$), ferric nitrate $\text{Fe}(\text{NO}_3)_3 \cdot 9\text{H}_2\text{O}$ (purity $\geq 99.0\%$) and manganese nitrate solution $\text{Mn}(\text{NO}_3)_2$ (purity $49.0\text{--}51.0\%$) were separately dissolved in an appropriate amount of 0.2 molar concentration. Citric acid and ethyleneglycol were then added in concentrations of 1.5 M and 2.25 M respectively. Citric acid ($\text{C}_6\text{H}_8\text{O}_7 \cdot \text{H}_2\text{O}$, purity $\geq 99.5\%$) as the complexing agent, ethylene glycol $(\text{CH}_2\text{OH})_2$, purity $\geq 99.5\%$ as the surfactant and deionized water as the solvent solutions were mixed together and the entire solution was stirred constantly at 100°C for 5 to 6 hours to form homogeneous solutions and obtained a transparent stable solution. About 5 hours later, the viscosity of the system increased and the mobility was lost, leading to the formation of viscous wet gel [7].

After the intensive drying in the furnace oven at 400°C for 3 hours, the resulting material appears in black powder form. A short-live digestion of the sample was observed due to the reaction of the nitrates and the formation of the manganite perovskite material close to 250°C [7]. The obtained material then made in fine powder which were subsequently annealed under three different calcination temperatures in air. The samples were annealed in a programmable box furnace oven at 800°C and 1000°C . The temperature was held for a period of 6 to 6.5 hours. Finally these samples were again ground for structural and magnetic characterizations.

[Chapter 5: Synthesis of $\text{La}_{0.67}\text{Sr}_{0.33}\text{Mn}_{1-x}\text{Fe}_x\text{O}_3$ ($x=0.15, 0.25$ and 0.35) materials prepared by Sol-Gel method]

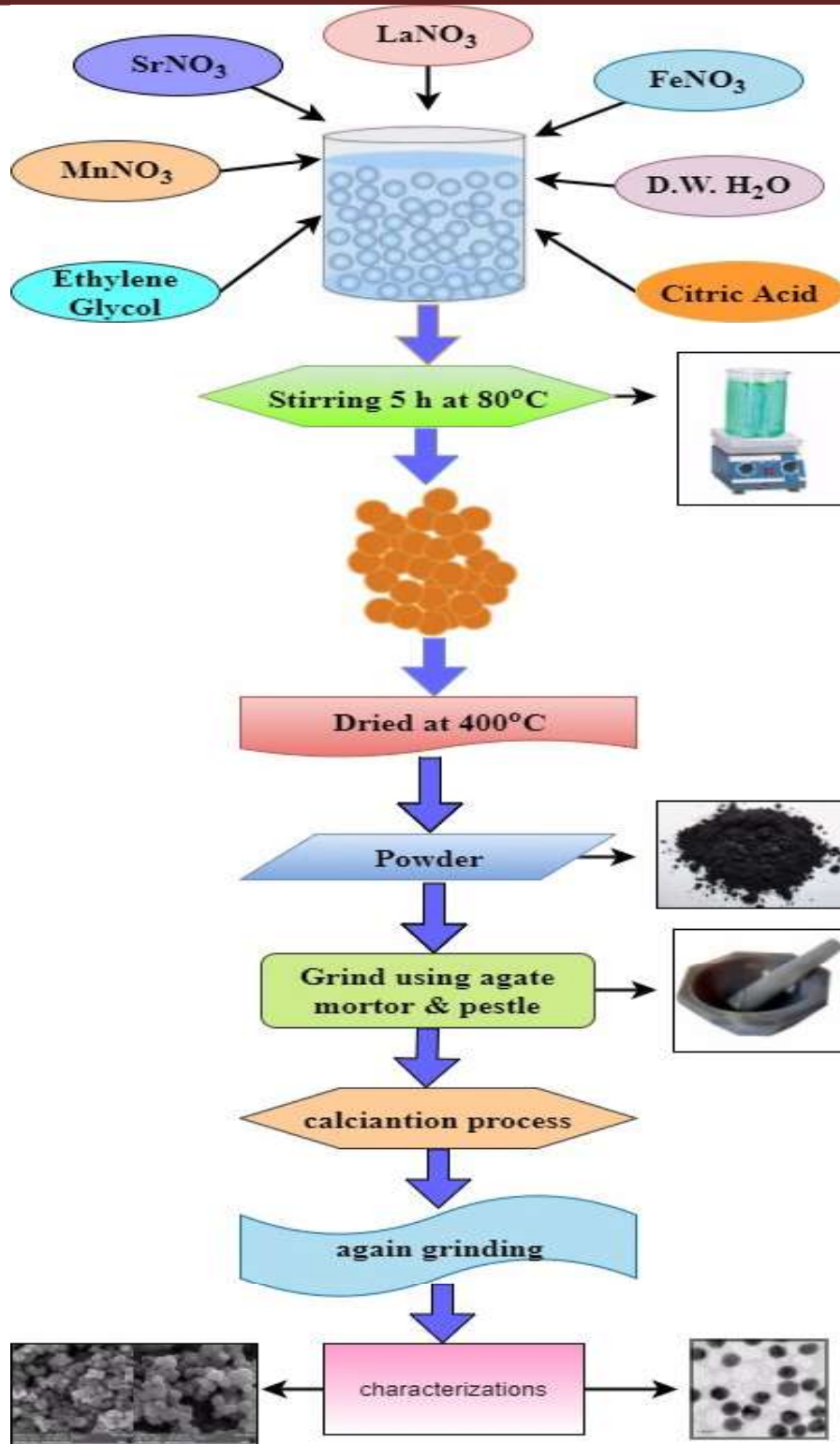


Fig. 5.3: Flow chart of the preparation of Fe doped LaSrMnO_3 by sol-gel technique.

[Chapter 5: Synthesis of $\text{La}_{0.67}\text{Sr}_{0.33}\text{Mn}_{1-x}\text{Fe}_x\text{O}_3$ ($x=0.15, 0.25$ and 0.35) materials prepared by Sol-Gel method]

The phase purity and nature of the crystal structure of the synthesized polycrystalline samples were studied by PANalytical X'pert Pro X-ray diffractometer using $\text{Cu-K}\alpha$ (1.5406 Å) radiation at room temperature. The X-ray diffraction patterns were fitted by Rietveld refinement using FullProf program in order to obtain structural parameters for each sample having different doping concentration at different temperature. The surface morphology of prepared samples was determined by scanning electron microscope (SEM) using JEOL JMS-5610LV and Oxford INCA Energy Dispersive analysis of X-ray (EDAX). The transmission electron microscopy (TEM) was determined by JEM-F200. The vibrational properties were studied by Raman spectroscopy using JOBIN YVON HORIBA-HR800 at room temperature. The study of magnetic properties of the samples was carried out by vibrating sample magnetometer (quantum SQUID) in the temperature range 0 K to 360 K. The results of the various measurements of the synthesized samples are explained sequentially in upcoming sections.

5.3 Results and Discussion

5.3.1 X-ray Diffraction (XRD)

The manganite perovskite structure of $\text{La}_{0.67}\text{Sr}_{0.33}\text{Mn}_{1-x}\text{Fe}_x\text{O}_3$ nanoparticles ($x= 0.15, 0.25$ and 0.35) at various calcined temperatures such as 800°C and 1000°C was confirmed utilizing PANalytical X'Pert Pro in the powder diffraction mode with $\text{CuK}\alpha$ radiation line. The 2θ range of X-ray intensity data were taken from 20° to 80° . The raw profile of powder diffraction pattern having different Fe doping concentration of LSMO nanoparticles are introduced in Figs. 5.4 and 5.5. As per the XRD investigation, all prepared nanocrystalline samples are in single phase without demonstrating any subsidiary or contamination phase and crystallize in the distorted perovskite structure.

[Chapter 5: Synthesis of $\text{La}_{0.67}\text{Sr}_{0.33}\text{Mn}_{1-x}\text{Fe}_x\text{O}_3$ ($x=0.15, 0.25$ and 0.35) materials prepared by Sol-Gel method]

The obtained X-ray diffraction data of the samples were refined for their structural and stoichiometric parameters utilizing the well known Rietveld method. The Rietveld (1969) technique was used for refining structural parameters (fractional coordinates, atomic displacement parameters, occupation factors and lattice parameters) using the FullProf software directly from entire powder diffraction patterns. The broad peak formed at $2\theta \sim 32.57^\circ$, which is recognized for LSMFO perovskite structure is used to calculate the crystallite size. The results display no structural transition and a negligible shift of peak positions with varying Fe^{3+} composition, since Mn^{3+} and Fe^{3+} ions have nearly a similar ionic radius [8]. The diffraction peaks corresponding to planes (012), (110) and (104) are in good concurrence with JCPDS data which shows that the LSMFO is formed in rhombohedral crystal structure with R-3c space group. The (202), (214) and (128) reflections indicate crystalline nature of the sample. The results further affirms that all prepared nanocrystalline samples are in single phase and Fe^{3+} ions can partially replace Mn ions to enter into the crystal lattice effectively. Some peaks corresponding to secondary phases were detected as trace from XRD of the samples obtained from ball milled route. All impurity phases vanished in XRD pattern obtained from sol-gel method. We can argue that the all nitrates are completely dissolved and the chemical reaction is completed during this synthesis process. The secondary phase obtained might be due to the $\text{La}(\text{OH})_3$. This phase arises due to variation in atomic size of the La and Sr. The phase relations for sol-gel prepared samples show no marked variation as compared to those obtained by ball milling method. However, it is evident that the phase relation as obtained by sol gel process showed much narrower single phasic rhombohedral phase as compared to the ball milled synthesized compound. The XRD peaks of all the prepared samples by ball milled route are slightly shifting to lower side as compared to SG process due to same ionic radius of the Fe and

[Chapter 5: Synthesis of $\text{La}_{0.67}\text{Sr}_{0.33}\text{Mn}_{1-x}\text{Fe}_x\text{O}_3$ ($x=0.15, 0.25$ and 0.35) materials prepared by Sol-Gel method]

Mn ions. The main prominent peak (110) for all the samples is aligned at $2\theta \sim 32.7^\circ$ in BM route and same is slightly shifted to the 32.66° in sol-gel method. This shifting of peak towards the lower side reveals that the strain is induced from doping ions and also indicating an increase in the degree of long range order in the perovskite lattice. The shifting towards the lower 2θ , with Fe doping in both synthesis process indicates the increase in unit cell volume. This is due to the similar ionic radius of Fe and Mn ions at B-site and reduction in internal pressure which expands volume of the unit cell and in all directions enhancement of the unit cell parameters. A close observation of the XRD data indicates that prominent diffraction peak shifts towards lower angle side.

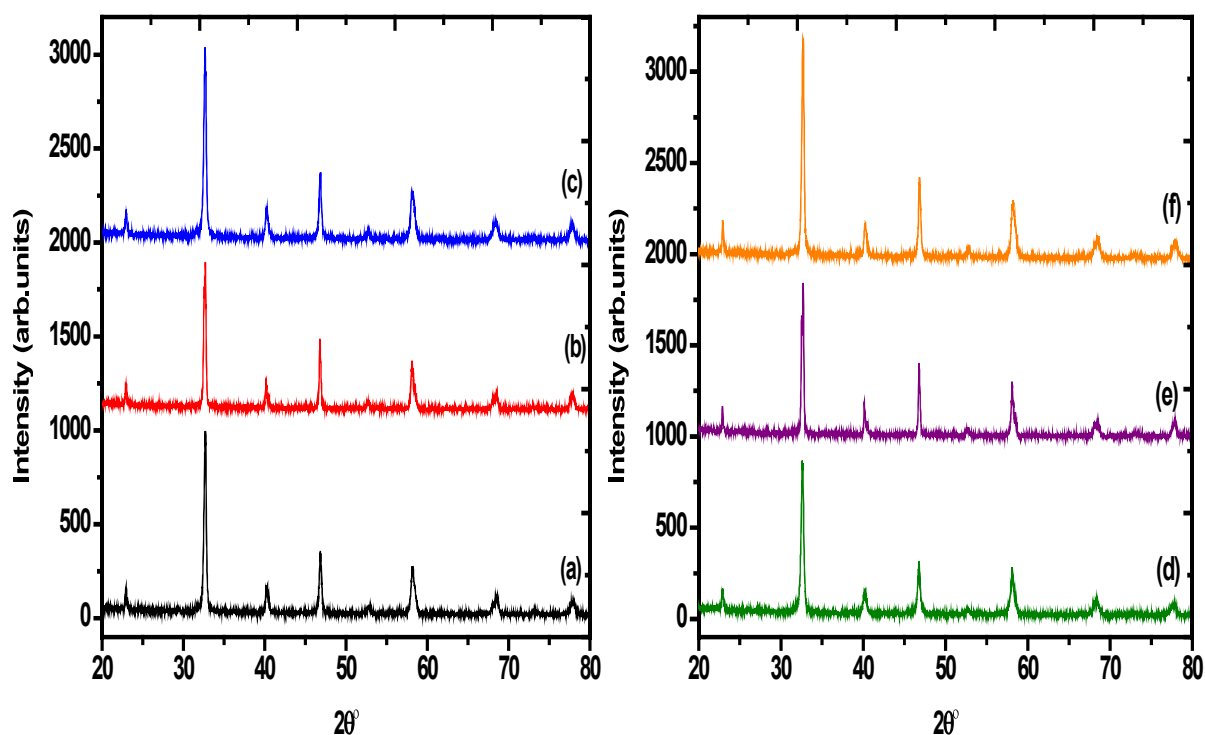


Fig. 5.4: The X-ray diffraction pattern of Fe doped $\text{La}_{0.67}\text{Sr}_{0.33}\text{Mn}_{1-x}\text{Fe}_x\text{O}_3$ manganite systems (a) $x=0.15-800^\circ\text{C}$ (b) $0.25-800^\circ\text{C}$ (c) $0.35-800^\circ\text{C}$ (d) $0.15-1000^\circ\text{C}$ (e) $0.25-1000^\circ\text{C}$ (f) $0.35-1000^\circ\text{C}$.

[Chapter 5: Synthesis of $\text{La}_{0.67}\text{Sr}_{0.33}\text{Mn}_{1-x}\text{Fe}_x\text{O}_3$ ($x=0.15, 0.25$ and 0.35) materials prepared by Sol-Gel method]

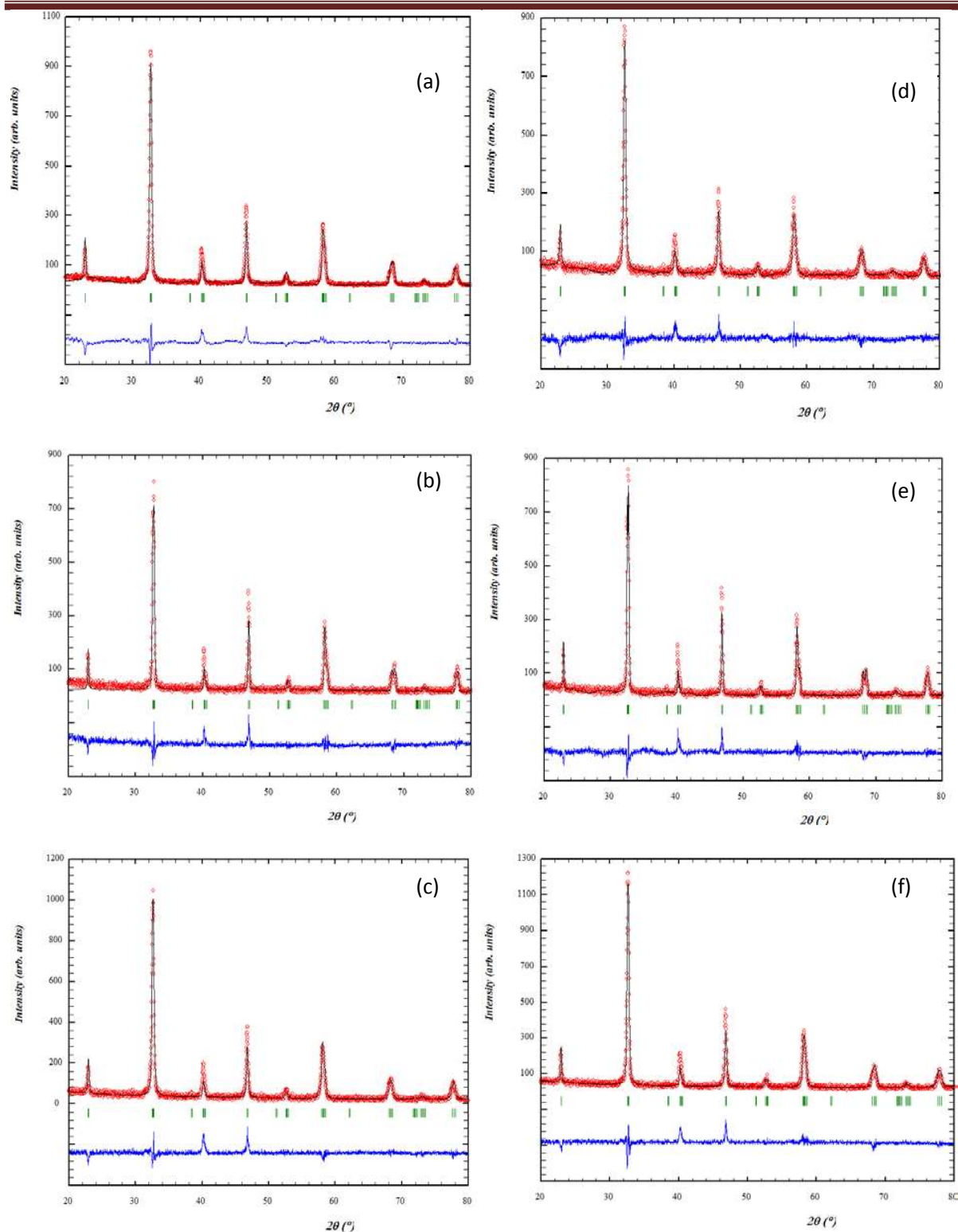


Fig.5.5: Rietveld refinement X-ray diffraction pattern of $\text{La}_{0.67}\text{Sr}_{0.33}\text{Mn}_{1-x}\text{Fe}_x\text{O}_3$ (a) $x=0.15$ -800°C (b) 0.25 -800°C (c) 0.35 -800°C (d) 0.15 -1000°C (e) 0.25 -1000°C (f) 0.35 -1000°C.

[Chapter 5: Synthesis of $\text{La}_{0.67}\text{Sr}_{0.33}\text{Mn}_{1-x}\text{Fe}_x\text{O}_3$ ($x=0.15, 0.25$ and 0.35) materials prepared by Sol-Gel method]

The Rietveld refined parameters R_p , R_{wp} , R_{exp} and χ^2 indicators were used to assess the quality of the refined structural models. Table 5.1 presents the lattice parameters, cell volume, atomic positions and average crystallite size of the prepared samples. The Table 1 clearly shows that all parameters of nanoparticles slightly increase with the increasing Fe content. Taking into account that Mn^{3+} and Mn^{4+} ionic radii are 0.65 and 0.53 Å, respectively [9, 10] and the ionic radius of Fe^{3+} ions is 0.645 Å. The hetero valent substitution of smaller Mn^{4+} ions by larger Fe^{3+} ions takes place according to the scheme $\text{La}_{0.773}+\text{Sr}_{0.232}+\text{Mn}_{0.773}+\text{Mn}_{0.23-y}+\text{Fe}_{y3}+\text{O}_{3-y/2}$ [9]. The cell volume and lattice parameters are in good match with the standard JCPDS data.

The doping of Fe^{3+} does not introduce noticeable lattice distortion [11,12]. Therefore, the lattice effects on magnetic and vibrational properties should be looked in these LSMFO samples. Comparative outcomes have been seen by other researchers [13-15]. The average crystallite size (D) was obtained utilizing the well known Debye Scherrer's equation $D= 0.9\lambda/\beta\cos\theta$, where λ is the incident X-ray wavelength, β is full width half maximum (FWHM) of the XRD peak corresponding to maximum intensity and θ represents the diffraction angle of the most intense peak in degrees [8]. The examination of XRD pattern is in good agreement with earlier reports available on doping of Fe in LSMO prepared using various routes.

[Chapter 5: Synthesis of $\text{La}_{0.67}\text{Sr}_{0.33}\text{Mn}_{1-x}\text{Fe}_x\text{O}_3$ ($x=0.15, 0.25$ and 0.35) materials prepared by Sol-Gel method]

Table 5.1 The Rietveld refinement structural parameters of Fe doped LSMO nanoparticles.

Sample	Lattice Parameter (Å)			Cell volume (Å ³)	Crystallite size D (nm)	Atomic position			Discrepancy Factor	
	a	b	c			x	y	z		
x=0.15 (800°C)	5.490	5.490	13.378	349.20	24	La/Sr	0.000	0.000	0.250	$R_p = 29.1$
						Mn/Fe	0.000	0.000	0.000	$R_{wp} = 24.0$
						O	0.531	0.000	0.250	$R_c = 27.4$
										$\chi^2 = 0.89$ GOF= 0.87
x=0.25 (800°C)	5.497	5.497	13.358	349.57	25	La/Sr	0.000	0.000	0.250	$R_p = 46.0$
						Mn/Fe	0.000	0.000	0.000	$R_{wp} = 41.5$
						O	0.539	0.000	0.250	$R_c = 28.2$
										$\chi^2 = 2.16$ GOF= 1.47
x=0.35 (800°C)	5.504	5.504	13.395	351.43	23	La/Sr	0.000	0.000	0.250	$R_p = 34.5$
						Mn/Fe	0.000	0.000	0.000	$R_{wp} = 32.4$
						O	0.579	0.000	0.250	$R_c = 25.8$
										$\chi^2 = 1.57$ GOF= 1.25
x=0.15 (1000°C)	5.501	5.501	13.411	351.47	21	La/Sr	0.000	0.000	0.250	$R_p = 37.7$
						Mn/Fe	0.000	0.000	0.000	$R_{wp} = 35.3$
						O	0.542	0.000	0.250	$R_c = 27.6$
										$\chi^2 = 1.63$ GOF= 1.27
x=0.25 (1000°C)	5.506	5.506	13.374	351.13	25	La/Sr	0.000	0.000	0.250	$R_p = 37.7$
						Mn/Fe	0.000	0.000	0.000	$R_{wp} = 34.4$
						O	0.540	0.000	0.250	$R_c = 27.5$
										$\chi^2 = 1.56$ GOF= 1.25
x=0.35 (1000°C)	5.500	5.500	13.380	350.53	26	La/Sr	0.000	0.000	0.250	$R_p = 37.7$
						Mn/Fe	0.000	0.000	0.000	$R_{wp} = 34.1$
						O	0.536	0.000	0.250	$R_c = 24.4$
										$\chi^2 = 1.91$ GOF= 1.39

[Chapter 5: Synthesis of $\text{La}_{0.67}\text{Sr}_{0.33}\text{Mn}_{1-x}\text{Fe}_x\text{O}_3$ ($x=0.15, 0.25$ and 0.35) materials prepared by Sol-Gel method]

Table 5.2 Optimized structural parameters of Fe doped LSMO using density functional theory.

Sample	Lattice Parameter, (Å)			Cell volume (Å ³)	Atomic position			
	a	b	c		x	y	z	
x=0.15 (800°C)	5.4789	5.4789	12.8899	335.10	La/Sr	0.000	0.000	0.250
					Mn/Fe	0.000	0.000	0.000
					O	0.468	0.000	0.250
x=0.25 (800°C)	5.4852	5.4852	12.8783	335.57	La/Sr	0.000	0.000	0.250
					Mn/Fe	0.000	0.000	0.000
					O	0.461	0.000	0.250
x=0.35 (800°C)	5.511	5.511	12.891	339.07	La/Sr	0.000	0.000	0.250
					Mn/Fe	0.000	0.000	0.000
					O	0.420	0.000	0.250

5.3.2 Field emission scanning electron microscope (FE-SEM)

Scanning electron microscope has been utilized to study the morphology of LSMFO samples with various resolutions to confirm the presence of nanoparticles of different sizes in samples. The surface morphology of the prepared nanoparticles was analyzed by field emission-scanning electron microscopy (FE-SEM) and corresponding images for all prepared Fe doped samples with different concentration ($x=0.15, 0.25$ and 0.35) at various calcination temperatures, for example, 800°C and 1000°C appear in Fig. 5.6. From the images, we observed that the most of the grains are in spherical shape with unvarying distribution.

[Chapter 5: Synthesis of $\text{La}_{0.67}\text{Sr}_{0.33}\text{Mn}_{1-x}\text{Fe}_x\text{O}_3$ ($x=0.15, 0.25$ and 0.35) materials prepared by Sol-Gel method]

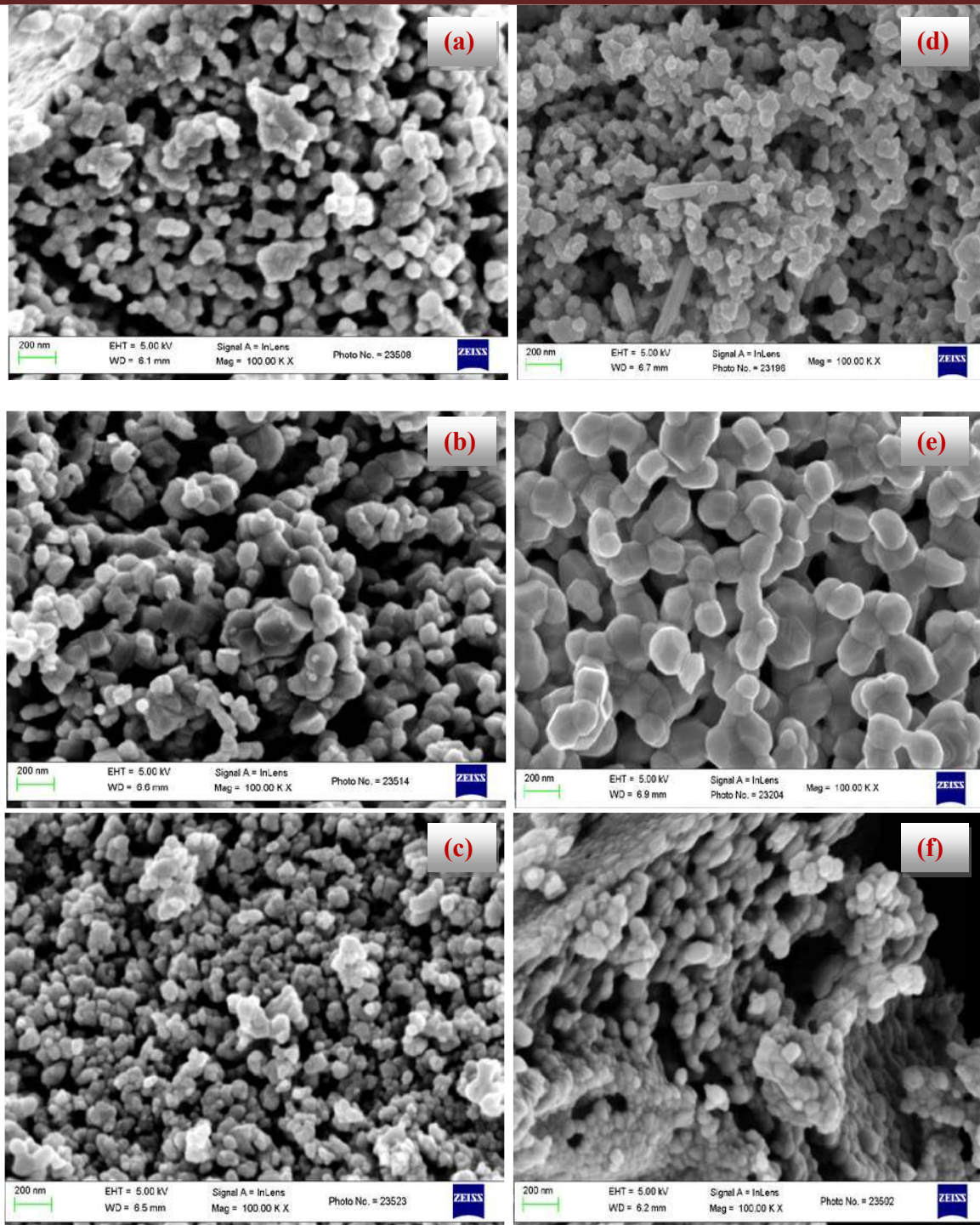


Fig. 5.6: FE-SEM micrograph of the prepared LSMFO samples with different doping compositions at various calcination temperatures (a) 0.15-800°C (b) 0.25-800°C (c) 0.35-800°C (d) 0.15-1000°C (e) 0.25-1000°C (f) 0.35-1000°C.

[Chapter 5: Synthesis of $\text{La}_{0.67}\text{Sr}_{0.33}\text{Mn}_{1-x}\text{Fe}_x\text{O}_3$ ($x=0.15, 0.25$ and 0.35) materials prepared by Sol-Gel method]

It is clearly observed that the morphology of the particles is in the nano sized range. The spherical particles appearing in the image are separated by the distance ranging from 33 – 50 nm. The average particle size confirms formation of nanoparticles by sol-gel method. The images are seen at the same magnification for all samples to reveal the nature of the particle size while the nature of agglomeration of nanoparticles at appropriate magnification. The images demonstrate clear grain boundaries as reported previously [16] and similar to ball milled method samples. The micrograph clearly shows that the grain size and their growth increase with increase of iron content without any porosity and voids in the prepared samples.

5.3.3 Transmission electron microscope (TEM)

We have performed transmission electron microscope (TEM) measurements for prepared LSMFO samples with Fe concentrations $x=0.15, 0.25$ and 0.35 at 800°C calcination temperatures. The TEM images presented in Figs. 5.7 show large homogeneity of the grain size for prepared samples. The TEM images show the clear morphology with the particle sizes in the range of 20–35 nm [17, 18].

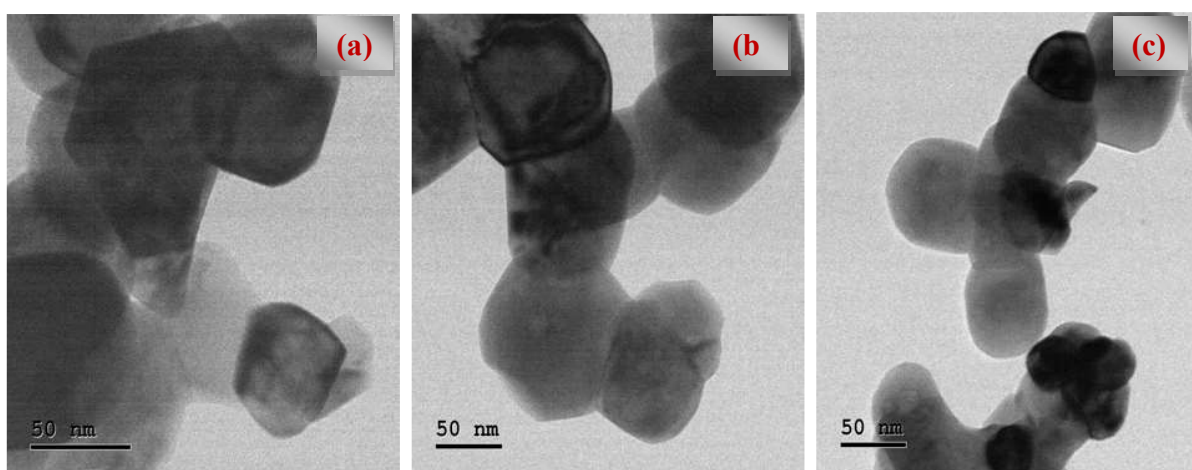


Fig. 5.7: The TEM analysis of LaSrMnFeO_3 prepared samples (a) $0.15\text{-}800^\circ\text{C}$ (b) $0.25\text{-}800^\circ\text{C}$ (c) $0.35\text{-}800^\circ\text{C}$.

[Chapter 5: Synthesis of $\text{La}_{0.67}\text{Sr}_{0.33}\text{Mn}_{1-x}\text{Fe}_x\text{O}_3$ ($x=0.15, 0.25$ and 0.35) materials prepared by Sol-Gel method]

5.3.4 Energy dispersive analysis of X-ray (EDAX)

A quantitative energy dispersive analysis of X-ray (EDAX) is used to determine the elemental analysis of the samples. The EDAX results presented in Figs. 5.8 and 5.9 reveal that the molar proportion of La, Sr, Mn, Fe and O which is relatively consistent with the nominal composition, suggesting that the obtained LSMFO sample is near stoichiometric. The spectra demonstrate that all samples are consistent with their elemental signals and stoichiometry as expected. The corresponding peaks of the samples are because of the La, Sr, Mn, Fe and O elements, whereas no any other impurity peak is detected which confirms the pure nature of prepared nanocrystalline samples [8, 19]. The composition obtained from EDAX spectra given in Table 5.3 agree with the expected values confirming desired stoichiometry of the prepared samples having various Fe doping concentration at different calcination temperatures.

Table 5.3 Atomic percent of the EDAX pattern recorded of studied samples.

Sample	Atomic (%)					Total
	Element					
	La	Sr	Mn	Fe	O	
0.15 (800°C)	14.68	5.48	17.16	2.90	59.78	100
0.25 (800°C)	16.90	5.32	17.22	5.39	55.18	100
0.35 (800°C)	11.97	5.18	10.15	5.98	66.71	100
0.15 (1000°C)	10.37	5.06	9.26	5.82	69.49	100
0.25 (1000°C)	15.92	5.20	16.95	5.45	56.48	100
0.35 (1000°C)	13.46	5.38	16.85	2.59	61.71	100

[Chapter 5: Synthesis of $\text{La}_{0.67}\text{Sr}_{0.33}\text{Mn}_{1-x}\text{Fe}_x\text{O}_3$ ($x=0.15, 0.25$ and 0.35) materials prepared by Sol-Gel method]

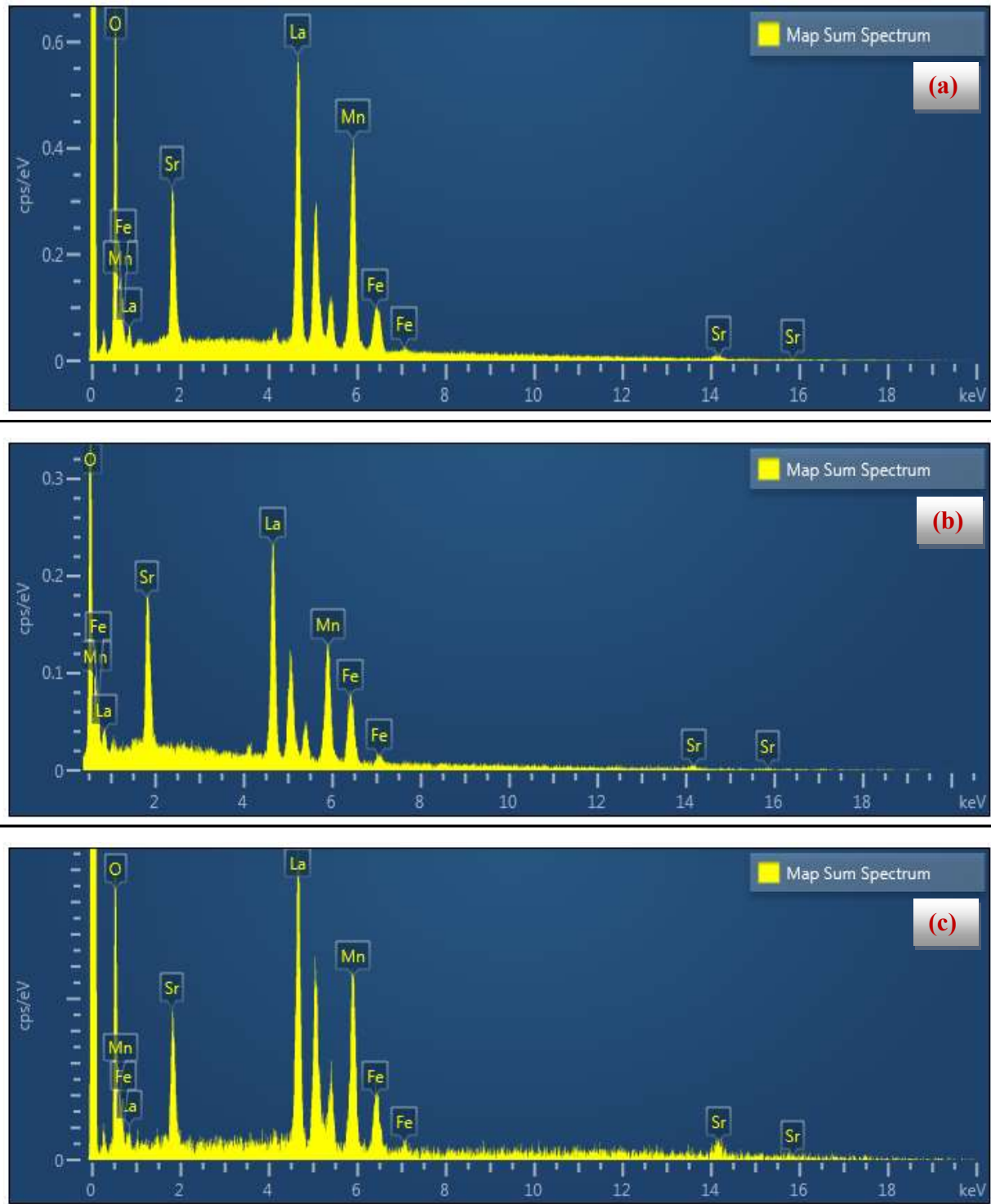


Fig. 5.8: EDAX analysis of prepared LSMFO samples (a) 0.15-800°C (b) 0.25-800°C (c) 0.35-800°C.

[Chapter 5: Synthesis of $\text{La}_{0.67}\text{Sr}_{0.33}\text{Mn}_{1-x}\text{Fe}_x\text{O}_3$ ($x=0.15, 0.25$ and 0.35) materials prepared by Sol-Gel method]

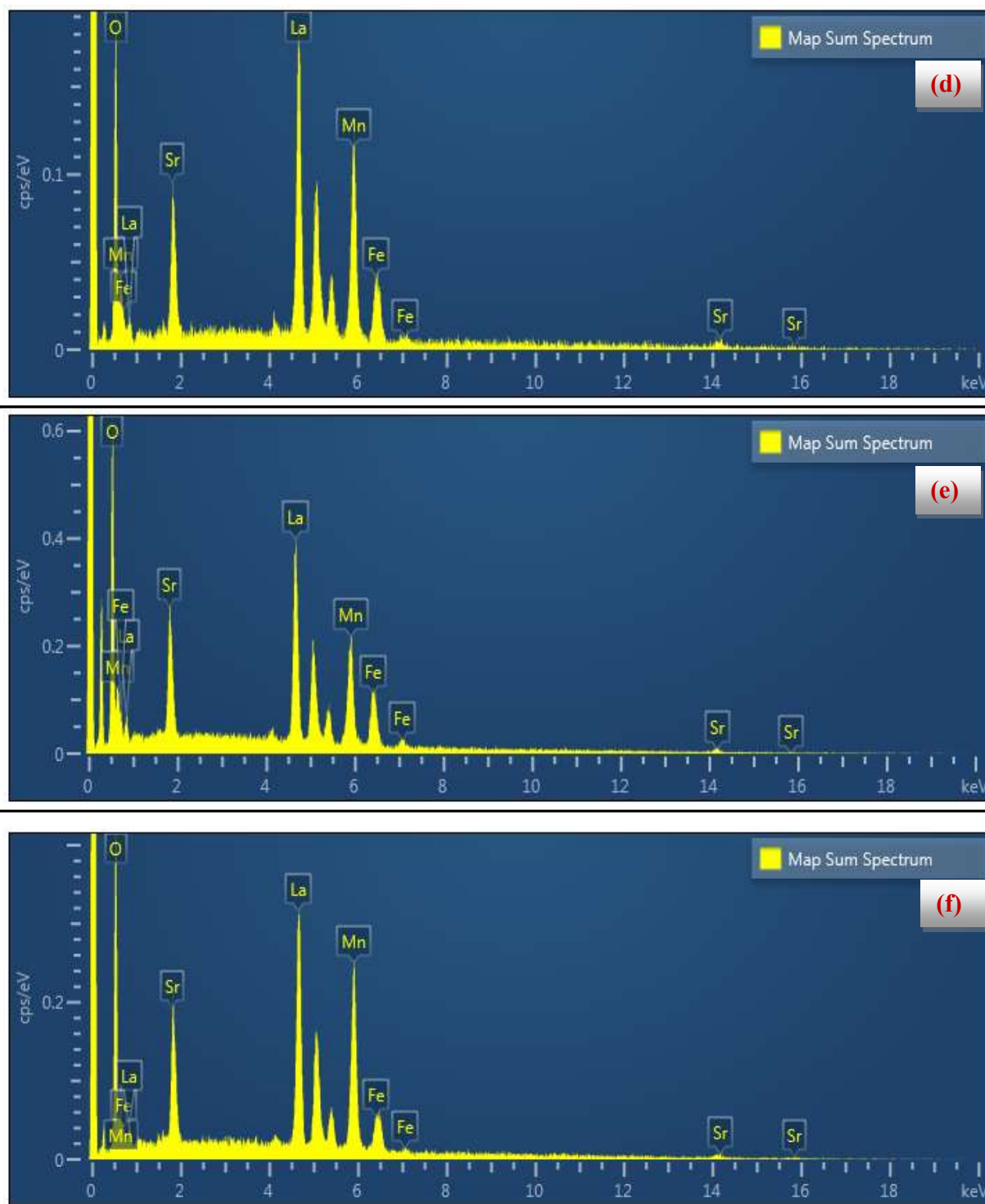


Fig. 5.9: EDAX analysis of prepared LSMFO samples (d) 0.15-1000°C (e) 0.25-1000°C (f) 0.35-1000°C.

[Chapter 5: Synthesis of $\text{La}_{0.67}\text{Sr}_{0.33}\text{Mn}_{1-x}\text{Fe}_x\text{O}_3$ ($x=0.15, 0.25$ and 0.35) materials prepared by Sol-Gel method]

5.3.5 Raman Spectroscopy

Synthesis of the manganite nanoparticles with controlled properties is still a major challenge. Raman spectroscopy has appeared as a dominant nondestructive tool to characterize the nanoparticles and used to perform vibrational analysis of a system [20-22]. Hence, the Raman spectroscopic measurements of samples synthesized using sol-gel method are examined and compared with the obtained data by planetary ball milling method. No phonon mode is dynamic in cubic perovskite structure while the orthorhombic or rhombohedral structure offers Raman-active phonon modes. It is accounted for that, the Raman dynamic A_{1g} and E_g are delicate to outside parameters [23]. The obtained Raman spectra of the prepared samples show confirmation of both the modes and also shifting to lower or higher wavenumber side is observed. General description of Raman spectroscopy is presented in previous chapters.

Our samples exhibit rhombohedral crystal structure with space group D_{3d}^6 (R-3c) like our prepared ball milling method. This structure can be obtained from the simple cubic perovskite by the rotation of the adjacent MnO_6 octahedra in the opposite directions around the $[111]_c$ cubic direction [8]. According to site group analysis, there are 30 vibrational modes in rhombohedral crystal structure with five Raman-active modes ($A_{1g} + 4E_g$) and eight infrared active ($3A_{2u} + 5E_u$) modes [8]. The spectrum of all prepared samples exhibit five broad bands between 209-230, 280-296, 400-440 and 675-700 cm^{-1} . As a consequence, it is found that the 209-230 cm^{-1} bands are A_{1g} modes only involve the motion of the oxygen ions in the C_2 sites, while other rest of the modes are the E_g mode arise both from oxygen site and La (Sr) site vibrations following Granado et al. [8, 24]. Raman spectra of $\text{La}_{0.67}\text{Sr}_{0.33}\text{Mn}_{1-x}\text{Fe}_x\text{O}_3$ samples are shown in Fig. 5.10. The weak mode at 281 cm^{-1} is E_g mode and antistretching mode at 675 cm^{-1} (out-of-phase stretching oxygen vibration) [25].

[Chapter 5: Synthesis of $\text{La}_{0.67}\text{Sr}_{0.33}\text{Mn}_{1-x}\text{Fe}_x\text{O}_3$ ($x=0.15, 0.25$ and 0.35) materials prepared by Sol-Gel method]

It is possible that the distortion of the oxygen sublattice results from two distinct steps: first, the oxygen neighboring to the substitutional ions are displaced directly by the stress produced by the substituent. Secondly, this displacement can lead to a localization of the e_g electrons around the substitutional ion, stimulating an additional long-range distortion of the oxygen sublattice by the JT effect [26]. The Raman peak with higher intensity is observed for 698 cm^{-1} while the same is shifted to 700 cm^{-1} at room temperature. This shift corresponded to tilt of MnO_6 octahedral [27].

The analysis of Raman spectra helps to understand the JT distortion. The number of phonon modes of LSMFO are less in rhombohedral than the orthorhombic phase. The intensity and width of the spectral line represent the deviation from the cubic structure and these spectra are representations of the Jahn–Teller contribution present in the system. The rhombohedral phase confirms the presence of Mn^{4+} than Mn^{3+} , as less amount of Mn^{4+} ion is sufficient to disturb the system and prefer the rhombohedral phase [28]. The spectra at $\sim 680\text{ cm}^{-1}$ appears is in great concurrence with the announced 690 cm^{-1} peak in the LSMO thin films and single crystals [29-31]. This mode can be related to an impurity mode, because of a second order Raman scattering process [27] and halfway uncovering of the phonon density of states (PDOS) [28]. Since, A_{1g} mode is of significance in context of R-3c phase can be utilized to comprehend the contribution as this mode is responsible for the rhombohedral distortion.

The Raman active A_{1g} mode traced out at 224 cm^{-1} in ball milled route is shifted to the 269 cm^{-1} in sol-gel process. We can see the slight difference in the mode frequencies of all prepared samples at 300K. The hardening of all modes is closely related to the magnetic transition in these materials. We believed that slight deviation of A_{1g} and E_g modes is thus associated with the spin lattice interaction in spin-ordered ferromagnetic phase. This conclusion

[Chapter 5: Synthesis of $\text{La}_{0.67}\text{Sr}_{0.33}\text{Mn}_{1-x}\text{Fe}_x\text{O}_3$ ($x=0.15, 0.25$ and 0.35) materials prepared by Sol-Gel method]

agrees with earlier report related FM ordering in manganites [32]. Moreover, the substitution of the La^{3+} ion by divalent Sr may induce a loss of oxygen in the samples that would induce additional modification in the octahedral distortions [32]. However, because the concentration of oxygen in our samples cannot be measured, it is not possible to have an estimate of this effect. The slight deviation of the A_{1g} phonon mode with increasing internal pressure is an indication of a stability in the electron phonon coupling strength and hence the less distortion of the octahedron. Further, the E_g modes show slight deviation from mode assignment for those parent and other divalent doped manganites. The slight deviation of the E_g modes which corresponds to the Mn-O bond from the frequency mass relationship for a rigid oscillator the high frequency vibrations would be assigned to the internal modes of MnO_6 octahedra. Amongst internal modes (the stretching motion of Mn-O bond is expected to have the highest frequency followed by the distortional vibrational of the O-Mn-O bond angle [33].

The results of the all prepared sample recorded to study the Raman spectra of the sample using Jobin-Yvon Horiba LABRAM-HR 800 visible micro-Raman instrument at room temperature is shown in Fig. 5.10.

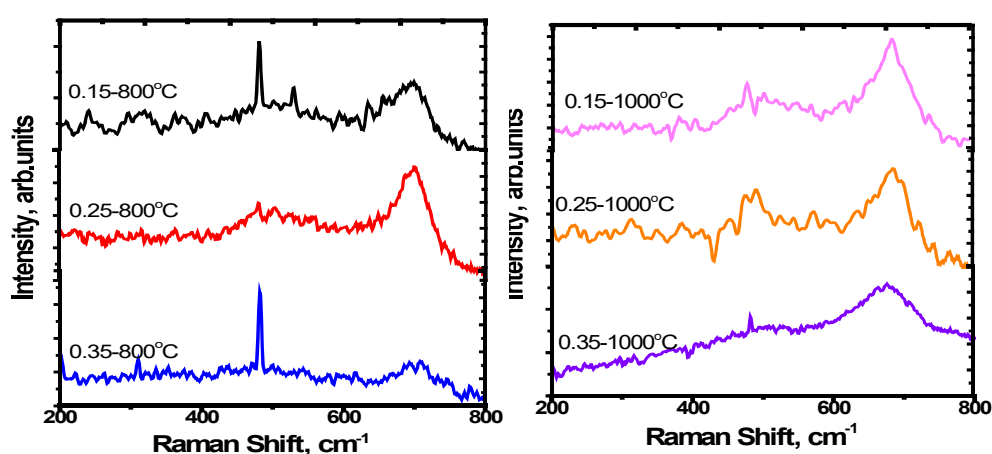


Fig. 5.10: Raman spectra of the $\text{La}_{0.67}\text{Sr}_{0.33}\text{Mn}_{1-x}\text{Fe}_x\text{O}_3$ ($x=0.15, 0.25$ and 0.35) manganite system at room temperature (300K).

[Chapter 5: Synthesis of $\text{La}_{0.67}\text{Sr}_{0.33}\text{Mn}_{1-x}\text{Fe}_x\text{O}_3$ ($x=0.15, 0.25$ and 0.35) materials prepared by Sol-Gel method]

Softening of mode near 700 cm^{-1} is a consequence of increased cell volume or increase in Mn-O distance. Temperature dependant Raman modes for all samples are summarized in Table 5.4. These modes are in good agreement with the reported data, confirming the particles in nano sized and single magnetic domain. The A_{1g} and E_g modes are related to the MnO_6 octahedra due to JT distortion in these systems [8]. It is observed that the A_{1g} mode is due to rotation while the E_g modes are due to the bending of MnO_6 octahedra. There is a good agreement with the earlier reports [8]. The peaks appear in samples synthesized by sol-gel method are more evident and intense than the planetary ball milling methods.

Table 5.4 The Raman active frequency mode of LaSrMnFeO_3 nanoparticles.

Sample	300 K			
	A_{1g}	E_g	E_g	E_g
0.15 (800°C)	209	296	405	699
0.25 (800°C)	221	281	409	700
0.35 (800°C)	221	290	428	693
0.15 (1000°C)	219	296	407	689
0.25 (1000°C)	230	313	414	696
0.35 (1000°C)	224	296	438	675

Raman spectroscopy can be an ideal way to find any impurities in the samples and may be more efficient than X-ray diffraction and energy dispersive analysis techniques [34, 35]. The

[Chapter 5: Synthesis of $\text{La}_{0.67}\text{Sr}_{0.33}\text{Mn}_{1-x}\text{Fe}_x\text{O}_3$ ($x=0.15, 0.25$ and 0.35) materials prepared by Sol-Gel method]

DE mechanism based on the large Hund coupling between e_g and t_{2g} electrons is insufficient to explain the CMR behavior [36]. Meanwhile, it states that contributions arising from dynamic JT splitting are helpful to explain the CMR behavior [37]. Our results present the illumination on the mechanism of JT distortion and effect on the Raman modes which helps to describe the different phenomena of colossal magnetoresistive material.

5.4 Density Functional Theory

The main aim of the present study is to find a correlation between calculated and experimentally obtained properties of Fe doped LSMO samples prepared using ball milling and sol-gel methods to find the process of formation by calculating the formation energy, structural, electronic and vibrational properties. While the optimization of structure with experimentally obtained structural parameters of all samples gives information about the formation, the spin polarized electronic calculations gives information about electronic as well as magnetic properties of samples.

Ab-initio calculations in the present study for $\text{La}_{0.67}\text{Sr}_{0.33}\text{Mn}_{1-x}\text{Fe}_x\text{O}_3$ ($x=0.15, 0.25$ and 0.35) have been performed within the local spin density approximation (LSDA) to the exchange correlation potential within the framework of density functional theory using the Vienna ab-initio simulation package (VASP). We have used a computational unit cell containing of LaSrMnFeO_3 formula units (i.e. 30 atoms) to simulate the R-3c phase within the ferromagnetic (FM) orderings. We have fully relaxed the cell shape (i.e., lattice parameters a , b , and c as well as the corresponding angles between them) and all internal structural degrees of freedom (all atomic positions). This complete geometrical optimization allowed us to tread the structural path of the R-3c phases. All the input parameters such as cut off energy, k-mesh etc., are used same as used

[Chapter 5: Synthesis of $\text{La}_{0.67}\text{Sr}_{0.33}\text{Mn}_{1-x}\text{Fe}_x\text{O}_3$ ($x=0.15, 0.25$ and 0.35) materials prepared by Sol-Gel method]

for ball milled samples in chapter. The starting crystal parameters of the $\text{La}_{0.67}\text{Sr}_{0.33}\text{Mn}_{1-x}\text{Fe}_x\text{O}_3$ have been taken from our present XRD data of corresponding samples.

The lattice, cell volume and related structural parameters of all samples found using optimization of the structure obtained from density functional theory are presented in Table 5.2. The optimization of a structure is to find minimum energy configuration. We have performed DFT calculations for selected systems. Fig. 5.11 presents the optimization curves of selected structures with respect to lattice parameters and energy cutoff values. Table 5.2 clearly depicts a good comparison between the experimentally and DFT calculated values except cell volume mainly due to *c* lattice parameter. The electronic properties of the $\text{La}_{0.67}\text{Sr}_{0.33}\text{Mn}_{1-x}\text{Fe}_x\text{O}_3$ (LSMFO) samples were carried out by first principle calculation using density functional theory (DFT) and compared with the obtained own experimental data. To understand the electronic properties of Fe doped $\text{La}_{0.67}\text{Sr}_{0.33}\text{Mn}_{1-x}\text{O}_3$, we have also calculated the electronic band structure at Γ -M-A-L- Γ symmetry points in irreducible Brillouin zone with Fermi level set at zero and presented then in Fig. 5.12. All samples show the metallic characteristics like ball milled method. The band structure contains all usual features of the manganites in general and ball milled samples presented in previous chapter in particular. The formation energy is calculated using Hess law discussed in previous chapter. The large negative value of formation energy confirms the formation of stable samples. Table 5.5 and Fig. 5.13 present the formation energy of three samples which clearly depict that all samples have negative formation energy indicating possibility of formation of Fe doped LSMO. However, the sample with $x=0.15$ Fe concentration has highest possibility due a very high negative formation energy. The ball mill method also has similar conclusion. We have calculated electronic band structure and density of states.

[Chapter 5: Synthesis of $\text{La}_{0.67}\text{Sr}_{0.33}\text{Mn}_{1-x}\text{Fe}_x\text{O}_3$ ($x=0.15, 0.25$ and 0.35) materials prepared by Sol-Gel method]

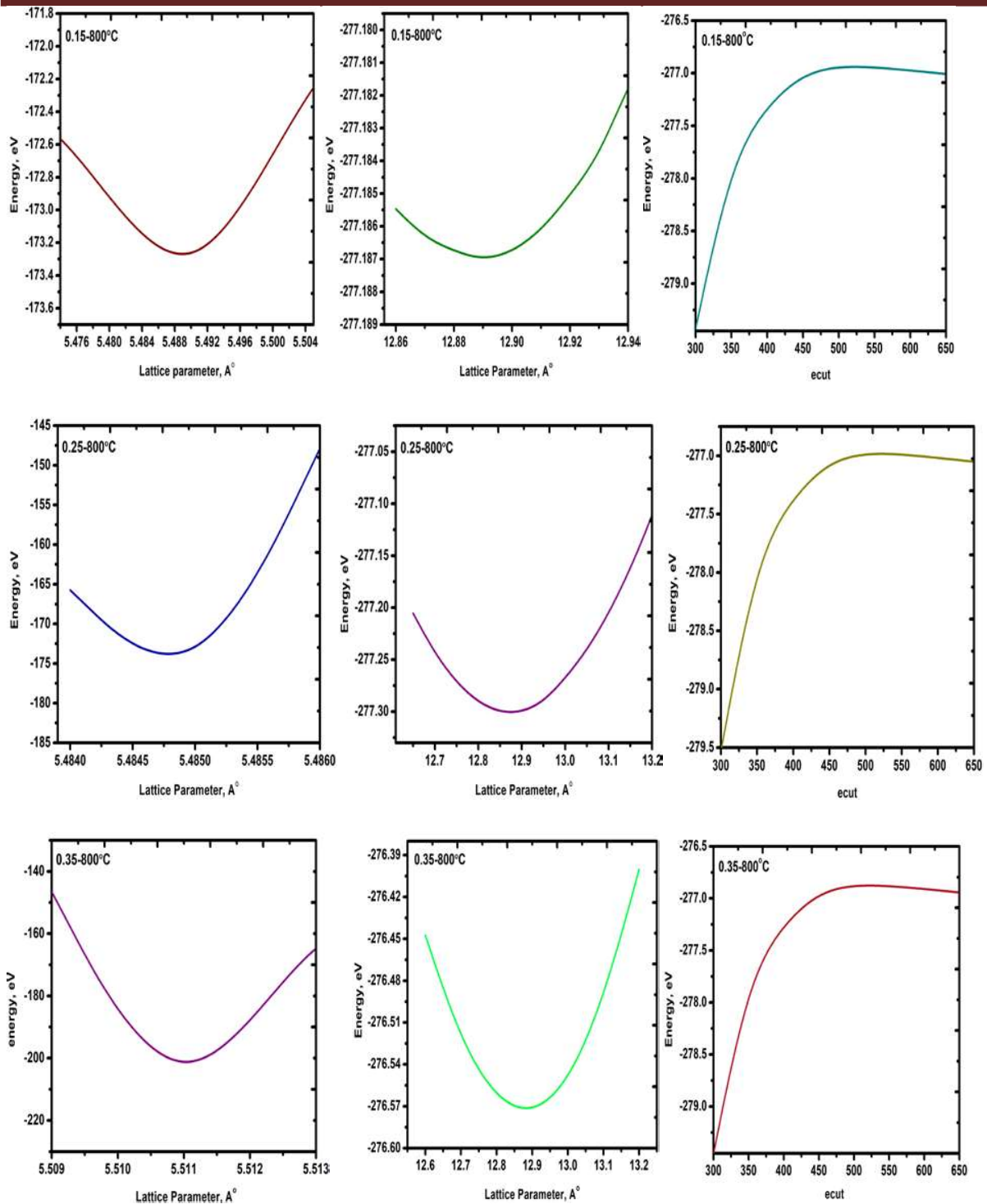


Fig. 5.11: Lattice parameter optimization and convergence of energy using density functional theory.

[Chapter 5: Synthesis of $\text{La}_{0.67}\text{Sr}_{0.33}\text{Mn}_{1-x}\text{Fe}_x\text{O}_3$ ($x=0.15, 0.25$ and 0.35) materials prepared by Sol-Gel method]

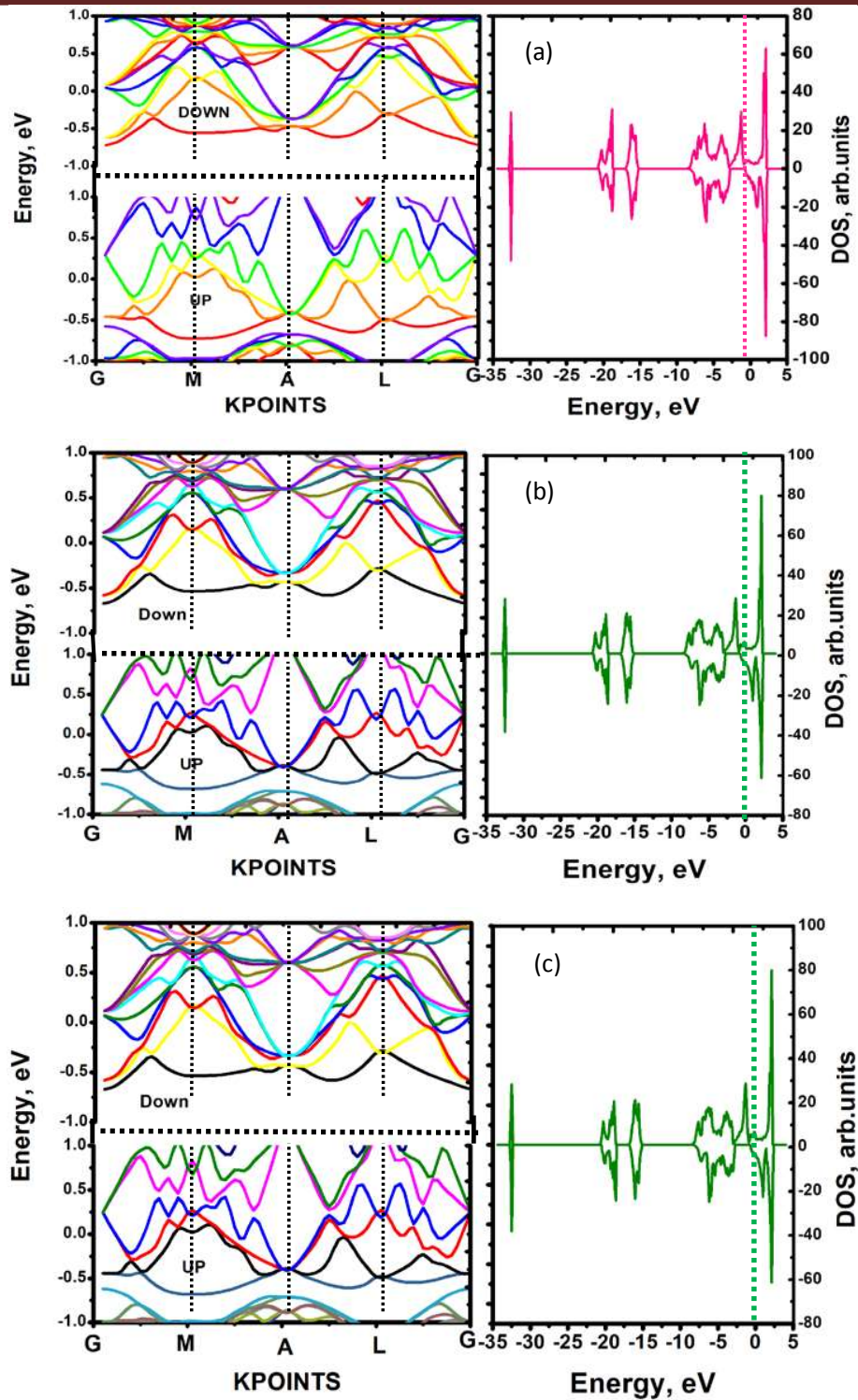


Fig. 5.12: Electronic band structure and total density states of Fe doped LSMO samples (a) 0.15-800°C (b) 0.25-800°C (c) 0.35-800°C.

[Chapter 5: Synthesis of $\text{La}_{0.67}\text{Sr}_{0.33}\text{Mn}_{1-x}\text{Fe}_x\text{O}_3$ ($x=0.15, 0.25$ and 0.35) materials prepared by Sol-Gel method]

Fig. 5.12 presents the density of states of Fe doped LSMO prepared using sol-gel method clearly shows that the majority spin metallicity in LSMFO results from the broad Mn 3d and O 2p hybridized states. The LSMFO DOS exhibit a half-metallic character with a spin minority line ball milled samples. The LSDA model provides a good description of the spin-dependent electronic properties. It can be same from the DOS spectra of Fe doped LSMO for Fe concentration of $x=0.15$ that the contribution of majority-spin channel to the peak of the density of states near the Fermi level is shifted by 0.05. This shift is also observed for $x=0.25$ and 0.35 Fe concentration. However, the contribution of the minority-spin channel to the DOS near the Fermi level for $x=0.15$ -800°C changes by about 0.23 for all considered concentration. The electronic states in band structure and density of states are the consequence of hybridization of atomic orbitals due to cation and anion.

We have also calculated the total magnetic moment of the Mn atoms which are surrounded by different cationic environment. We have not listed individual the contribution from La, Sr and O atoms to the total magnetic moment of the unit cell. The calculated magnetic moment of the unit cell is 16.465, 16.584 and 19.474 μ_B for $x=0.15, 0.25$ and 0.35 respectively, which are consistent with earlier report [38]. The enhancement of magnetic moments can be attributed to the change of complex interaction between Mn atoms and other atoms mainly the O atoms induced by octahedral rotation and deformation [39]. The average magnetic moment on the Mn atoms increase from 2.56, 2.58 and 2.62 μ_B for $x=0.15, 0.25$ and 0.35 respectively like ball milling method [40]. However, the magnetic moment value in the case of SG method is slightly higher.

We have also performed the first principle calculation of Raman modes of Fe doped LSMO samples annealed at 800°C for Fe concentration of $x= 0.15, 0.25$ and 0.35 and presented

[Chapter 5: Synthesis of $\text{La}_{0.67}\text{Sr}_{0.33}\text{Mn}_{1-x}\text{Fe}_x\text{O}_3$ ($x=0.15, 0.25$ and 0.35) materials prepared by Sol-Gel method]

them in Table 5.6. The phonon calculations to obtain the Raman mode frequencies using density functional theory are performed for three samples. The concentration of Fe is varied at a fixed calcinations temperature. There is a reasonably good agreement with the experimental data of SG prepared samples except for the highest E_g mode. However, the trend of variation is consistent with other calculations [41-43]. The use of Hubbard parameter U or hybrid functional may lead to better prediction of phonon modes. The calculated phonon frequencies show a shift in both A_{1g} and E_g modes after Fe doping similar to ball milling case. The shift in frequency is due to the changes in bond angle and bond length responsible for MnO_6 octahedra distortion.

Table 5.5 The calculated formation energy ΔH_F (eV) of Fe doped LaSrMnO_3 prepared by sol-gel method.

Sample	Formation energy (eV)
$x=0.15$ at 800°C	-5.120
$x=0.25$ at 800°C	-3.560
$x=0.35$ at 800°C	-1.140

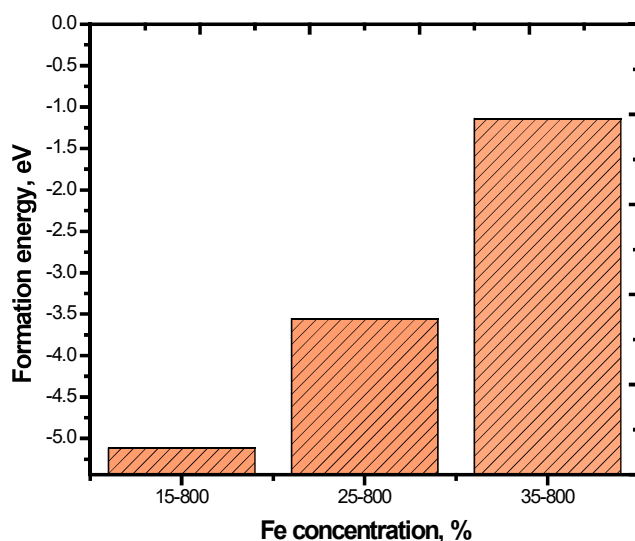


Fig. 5.13: Formation energy of $x=0.15, 0.25$ and 0.35 at 800°C .

[Chapter 5: Synthesis of $\text{La}_{0.67}\text{Sr}_{0.33}\text{Mn}_{1-x}\text{Fe}_x\text{O}_3$ ($x=0.15, 0.25$ and 0.35) materials prepared by Sol-Gel method]

Table 5.6 The Raman active frequency mode of LaSrMnFeO_3 using density functional theory. The bracket data are experimental value.

Sample	300 K			
	A_{1g}	E_g	E_g	E_g
0.15 (800°C)	210 (209)	301 (296)	413 (405)	628 (699)
0.25 (800°C)	214 (221)	294 (281)	410 (409)	614 (700)
0.35 (800°C)	219 (221)	264 (290)	436 (428)	510 (693)

[Chapter 5: Synthesis of $\text{La}_{0.67}\text{Sr}_{0.33}\text{Mn}_{1-x}\text{Fe}_x\text{O}_3$ ($x=0.15, 0.25$ and 0.35) materials prepared by Sol-Gel method]

5.5 Conclusion

Manganites that belong to strongly correlated electrons family possess various interesting properties due to variety of phases with unusual spin, charge, lattice degrees of freedom and orbital order. Much effort has been paid to the compounds $\text{R}_{1-x}\text{A}_x\text{Mn}_{1-y}\text{M}_y\text{O}_3$, where it is expected that the substitution of Mn ion, which is responsible for the double exchange may contribute to the knowledge of the basic mechanism of CMR as well as tuning of T_C .

In summary, we used sol-gel method to prepare the LSMO samples of different Fe compositions at different calcination temperature and studied its various properties. The X-ray diffraction pattern of all samples confirms the phase formation. The lattice parameters and cell volume of samples increased but are lower compared to that of prepared by planetary ball milling method. The density functional theory based first principle calculation is performed for samples with the help of their own structural data obtained for prepared samples. The optimized structures are used to calculate the mentioned physical properties and compared with experimentally obtained data.

Structural studies carried out using XRD measurement confirm the crystallinity of the prepared samples. The Rietveld refinement XRD patterns are good fitted using FullProf software. The results show that the lattice parameters, cell volume and average crystallite size increase with the Fe concentration. The morphological studies using field emission scanning electron microscope (FE-SEM) shows the grain are in spherical shape with non uniformity with the increase in average grain size with increasing Fe doping. The grain size ranges between 33-50 nm of prepared samples. The nanoparticle size is calculated by transmission electron microscope (TEM) which shows that the particle size increases with Fe concentration and its size

[Chapter 5: Synthesis of $\text{La}_{0.67}\text{Sr}_{0.33}\text{Mn}_{1-x}\text{Fe}_x\text{O}_3$ ($x=0.15, 0.25$ and 0.35) materials prepared by Sol-Gel method]

ranging between 20-35 nm. The results of the elemental analysis match well with stoichiometry of the compound.

The analysis of the results indicates the formation of nanoparticles with desired properties for further use in fabrication of devices. We have performed the vibrational properties using the Raman spectra. The peaks assigned in the Raman spectra are quite similar to the previous studies. The structural disorder near to grain boundary is observed, which affects the Zener double exchange mechanism due to changes in the stoichiometric composition and related parameters. Raman spectroscopy results show that the A_{1g} mode is of significance and took into account the R-3c phase can be utilized to comprehend the distortion as this mode includes the atomic motion responsible rhombohedral distortion. The experimentally observed feature of Raman spectra is consistent with the DFT calculated features.

The contribution of the majority-spin channel to the DOS near the Fermi level is shifted by 3.30 %, 10 % and 8 % respectively with compare to ball mill method for $x=0.15, 0.25$ and 0.35 . However, the contribution of the minority-spin channel to the DOS near the Fermi level changes by 5.45 %, 0.58 % and 3.20 % respectively withincreasing Fe content ($x = 0.15, 0.25$ and 0.35) compared to the ball milled method.

In ball milling and sol-gel methods, the formation energy is minimum for $x=0.15$ at 800°C . Experimental results suggest that the ball milling technique is successful in creating the LSMFO samples within the framework of mechanical synthesis. However, for better quality smaller particle size and lower calcination temperature for same configuration the sol-gel method is better.

[Chapter 5: Synthesis of $\text{La}_{0.67}\text{Sr}_{0.33}\text{Mn}_{1-x}\text{Fe}_x\text{O}_3$ ($x=0.15, 0.25$ and 0.35) materials prepared by Sol-Gel method]

References

1. C. J. Brinker and G. W. Scherer, "Sol-Gel Science", Academic Press, San Diego, pp. 912 (1990).
2. C. J. Brinker, A. J. Hurd, P. R. Schunk, C. S. Ashely, R. A. Cairncross, J. Samuel, K. S. Chen, C. Scotto and R. A. Schwartz, "Sol-Gel Derived Ceramic Films--Fundamentals and Applications", in: K. Stern (Ed.), Metallurgical and Ceramic Protective Coatings, Chapman and Hall, London, pp. 112 (1996).
3. T. Troczynski and Q. Yang, "Process for Making Chemically Bonded Sol-Gel Ceramics". U.S. Pat. No. 6, 284, 682 (2001).
4. T. Olding, M. Sayer and D. Barrow, "Ceramic Sol-Gel Composite Coatings for Electrical Insulation", Thin Solid Films, 581, pp. 398 (2001).
5. Y. Dimitriev, Y. Ivanova and R. Iordanova, J. of the University of Chemical Technology and Metallurgy, 43, 181 (2008).
6. M. Ashby, P. Ferreira and D. Schodek, Nanomaterials, Nanotechnologies and Design, Butterworth-Heinemann, 1st Ed. pp. 560 (2009).
7. N. D. Lipham, G. M. Tsoi, and L. E. Wenger, IEEE Transactions on Magnetics 43, (6) 3088 (2007).
8. N. M. Astik, H. Soni, P. K. Jha and V. Sathe, Physica B: Condensed Matter 541, 103 (2018).
9. Y. Shlapa, M. Kulyk, V. Kalita, T. Polek, A. Tovstolytkin, J. M. Greneche, S. Solopan and A. Belous, Nanoscale Research Letters 11, 24 (2016).
10. R. D. Shannon and C. T. Prewitt, Acta Crystallography B25, 925 (1969).
11. N. Kumar, H. Kishan, A. Rao and V. P. S. Awana, J. Alloy. Compd. 502, 283 (2010).
12. P. Nisha, S. S. Pillai, A. Darbandi, M. R. Varma, K.G. Suresh and H. Hahn, Mater. Chem. Phys. 136, 66 (2012).
13. M. Baazaoui, S. Zemni, M. Boudard, H. Rahmouni, A. Gasmi, A. Selmi and M. Oumezzine, Mater. Lett. 63, 2167 (2009).
14. Q. Huang, Z.W. Li, J. Li and C.K. Ong, J. Appl. Phys. 89, 7410 (2001).
15. V. Dayal and S. Keshri, Solid State Commun. 142, 63 (2007).

[Chapter 5: Synthesis of $\text{La}_{0.67}\text{Sr}_{0.33}\text{Mn}_{1-x}\text{Fe}_x\text{O}_3$ ($x=0.15, 0.25$ and 0.35) materials prepared by Sol-Gel method]

16. T. Raoufi, M. H. Ehsani and D. S. Khoshnoud, *J. Alloys Compd.* 689, 865 (2016).
17. S. Daengsakul, C. Thomas, I. Thomas, C. Mongkolkachit, S. Siri, V. Amornkitbamrung and S. Maensiri, *Nanoscale Res. Lett.* 4, 839 (2009).
18. N. D. Thorat, K. P. Shinde, S. H. Pawar, K. C. Barick, C. A. Betty and R. S. Ningthoujam, *Dalton Trans.* 41, 3060 (2012).
19. N. Astik, P. K. Jha and A. Pratap, *J. of Electronic Mater.* 47, 1937 (2018).
20. M. Fujii, T. Nagareda, S. Hayashi and K. Yamamoto, *Phys. Rev. B* 44, 6243 (1991).
21. X. L. Wu, Y. F. Mei, G. G. Siu, K. L. Wong, M. J. Stokes, C. L. Fu and X. M. Bao, *Phys. Rev. Lett.* 86, 3000 (2001).
22. D. C. Harris and M. D. Bertolucci, *Symmetry and spectroscopy: An introduction to vibrational and electronic spectroscopy.* Oxford University Press, New York: pp. 388 (1978).
23. P. K. Jha and M. Talati, *A computational study of the phonon dynamics of some complex oxides, Computational Materials*, Ed. Wilhelm U. Oster, Nova Science Publisher, New York, pp.177 (2009).
24. E. Granodo, N.O. Moreno, A. Garcia, J.A. Sanjurjo, C. Rettori, I. Torriani, S.B. Oseroff, J. J. Neumeier, K. J. McClellan, S. W. Cheong and Y. Tokura, *Phys. Rev. B* 58, 11435 (1998).
25. I. A. A. Latif, A. A. Ismail, H. Bouzid and A. Al-Hajry, *J. of Magn. Mag. Mater.* 393, 233 (2015).
26. F. A. Mir, M. Ikram and R. Kumar, *Phase Transitions* 84, 167 (2011).
27. R. Ren, Y. Ren, X. Li, L. Wen, S. Chen, Z. Wu and R. Xu, *Progress in Natural Science: Mater. International* 26, 173 (2016).
28. Y. Tokura, *Colossal Magnetoresistive Oxides*, Gordon and Breach Science Publishers, the Netherlands, pp. 358 (2000).
29. D. Bormann, R. Desfeux, F. Degave, B. Khelifa, J. F. Hamet, J. Wolfman, *Phys. Status Solidi B* 215, 691 (1999).
30. V. A. Dediu, J. Lopez, F. C. Matocotta, P. Nozar, G. Ruani, R. Zamboni and C. Taliani, *Phys. Status Solidi B* 215, 625 (1999).

[Chapter 5: Synthesis of $\text{La}_{0.67}\text{Sr}_{0.33}\text{Mn}_{1-x}\text{Fe}_x\text{O}_3$ ($x=0.15, 0.25$ and 0.35) materials prepared by Sol-Gel method]

31. V. B. Podobedov, A. Weber, D. B. Romero, J. P. Rice and H. D. Drew, *Solid State Commun.* 105, 589 (1998).
32. P. T. Phong, S. J. Jang, B. T. Huy, Y. I. Lee, I. J. Lee, *J. Mater. Sci. Mater. Electron* 24, 2292 (2013).
33. N. Dodiya and D. Varshney, *J. Mol. Str.* 1031, 104 (2013).
34. T. Fukumura, M. Ohtani, M. Kawasaki, Y. Okimoto, T. Kageyama, T. Koida, T. Hasegawa, Y. Tokura and H. Koinuma, *App. Phys. Lett.* 77, 3426 (2002).
35. A. Venimadha, K. A. Yates and M. G. Blamire, *J. of Combinatorial Chem.* 7, 85 (2005).
36. A. J. Millis, P. B. Littlewood and B. I. Shraiman, *Phys. Rev. Lett.* 74, 5144 (1995).
37. V.G. Sathe, R. Rawat, A. Dubey, A. V. Narlikar and D. Prabhakaran, *J. Phys.: Condens. Matter* 21, 075603 (2009).
38. J. Li, *Scientific Reports* 6, 1 (2016).
39. P. Y. Vanina, A. A. Naberezhnov, V. I. Nizhankovskii and R. F. Mamin, *Journal: Physics and Mathematics* 2, 175 (2016).
40. W. X. Xianyu, B. H. Li, Z. N. Qian and H. M. Jin, *J. Appl. Phys.* 86, 5164 (1999).
41. M. Talati and P. K. Jha, *Int. J. Mod. Phys. B* 23, 4767 (2009).
42. M. V. Abrashev, A. P. Litvinchuk, M. N. Iliev, R. L. Meng, V. N. Popov, V. G. Ivanov, R. A. Chakalov and C. Thomsen, *Phys. Rev. B* 59, 4146 (1999).
43. P. T. Phong, S. J. Jang, B. T. Huy, Y. I. Lee and I. J. Lee, *J. Mater. Sci. Mater. Electron* 24, 2292 (2013).